Local buckling on large sandwich panels used in light aviation

M. Ginot, C. Bouvet, Bruno Castanié, Joël Serra, N. Mahuet

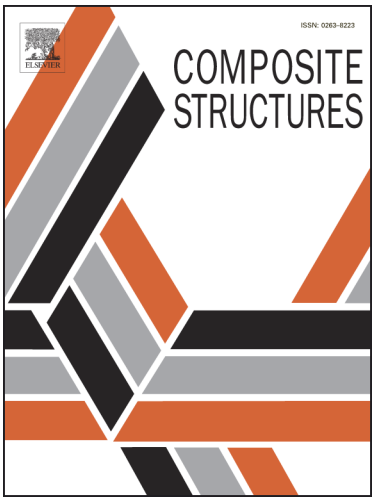

Local buckling on large sandwich panels used in light aviation: Experimental setup and failure scenarios.

M. Ginot, C. Bouvet, B. Castanié, J. Serra Testing, N. Mahuet Industrial

PII: S0263-8223(22)01171-0
DOI: https://doi.org/10.1016/j.compstruct.2022.116439
Reference: COST 116439

To appear in: *Composite Structures*

Received Date: 5 August 2022
Revised Date: 11 October 2022
Accepted Date: 26 October 2022

Please cite this article as: Ginot, M., Bouvet, C., Castanié, B., Serra Testing, J., Mahuet Industrial, N., Local buckling on large sandwich panels used in light aviation: Experimental setup and failure scenarios., *Composite Structures* (2022), doi: https://doi.org/10.1016/j.compstruct.2022.116439

Local buckling on large sandwich panels used in light aviation: Experimental setup and failure scenarios.

M. Ginot[a,b], C. Bouvet[b], B. Castanié[b,*], J. Serra[b], N. Mahuet[a]

[a] Elixir Aircraft, Rue du Jura, 17000 La Rochelle, France

[b] Institut Clément (ICA), Université de Toulouse, CNRS UMR 5312, INSA, ISAE-Supaéro, INSA, IMT Mines Albi, UPS, Toulouse, France

* Corresponding author: bruno.castanie@insa-toulouse.fr

Keywords: Sandwich structures; Local buckling; Wrinkling; Structural testing; Light aviation

Abstract

The design of light aircraft sandwich structures is driven by a local buckling phenomenon named “wrinkling” which can be the primary cause of failure of such structures. Structural tests using the VERTEX methodology were performed to access the wrinkling behaviour of 558x536 mm² technological sandwich specimens representative of the design used in light aviation. The operating principle of the VERTEX machine is the use of four hydraulic actuators to load a rectangular box structure, the upper part of the central box being closed by the sandwich under test. Thus, sandwich specimens were tested under compressive and shear loading. A wrinkling scenario was identified thanks to Stereo Digital Image Correlation and a high-speed camera. Wrinkling localisation is driven by mechanical and geometrical aspects. Experiments on wrinkling in sandwich panels remain rare in the literature at this level of the test pyramid for certification of aeronautical structures. This upper scale presents some advantages as it allows multiaxial loading and boundary conditions consistent with a lightweight aeronautical structure. Technological elements can also be added to study their

influence on the structure. The result will lead to interesting future investigations on the dialogue between experiments and models in a forthcoming paper.

1 Introduction

A sandwich structure consists of two thin, high-strength material skins that are separated by a thick, relatively weak, lightweight material, the core. Separating the skins by the core enhances the bending stiffness of such structures, without leading to a significant increase in mass. The skins carry in-plane loads and the core transfers load between the skins, essentially by transverse shear and normal stresses. Their high specific bending stiffness makes sandwich structures attractive and they have been widely used in aviation for more than a hundred years now [1]. They are being increasingly used for primary structures for light aviation (like the "Elixir" from Elixir Aircraft®, certified by the EASA in June 2020 [2]). However, the difference in mechanical and geometrical properties between skins and core induces several complex failure scenarios [3]. One of them, local buckling named "wrinkling", can be a primary cause of failure, especially on sandwich structures where the mechanical properties of the core are very low. Wrinkling is a local instability of the skins, which manifests itself when a sandwich structure is subjected to compression or shear loading. The buckling pattern takes the form of short-wavelength wrinkles in the skins, the length of which is of the order of the thickness of the sandwich [4]. In an industrial approach to structural sandwich structure design, an effective methodology for wrinkling sizing is under discussion and historic analytical formulas are still mainly used [5][6][7][8]. Even though less restrictive formulations have been developed recently [9][10][11]. A critical review of the literature and a benchmark study has shown that classical and more recent analytical formulas have limitations for recent sandwich structure designs [12]. These limits can be removed with numerical resolution as for the model

developed in [13] based on the Carrera Unified Formulation (C.U.F). In order to investigate the post-buckling behaviours of sandwiches, finite element modes have been developed [10]. More recently, studies have focused on the development of enriched finite element models [14] [15] where higher-order kinematics is adopted for the core. The non-linear solution uses the asymptotic numerical method (ANM). The principle of this method is to convert the system of non-linear equations into higher-order polynomial series. The model accurately predicts the critical loads as well as the bifurcated post-buckling branches while having a reduced computational time. These models are challenged by exact analytical solutions if available or by Finite Element results [16][12] but theoretical-experimental correlation must be the final validation step. However, reports of experimental tests on the wrinkling phenomenon are still scarce in the literature. Previous works have shown that the high sensitivity of compressive tests to boundary conditions and initial geometrical defects leads to difficulties in correlating experiments and models [5][4][17]. This is particularly true at the beam scale, which corresponds to most of the experimental studies in the literature. To improve the quality of testing, particular attention must be paid to mastering the boundary conditions, and to correct introduction of the compression load [5][18][19]. Some recommendations are also proposed in the ASTM standard C364-94 or the French NF T 54-604. Fagerberg [20] performed tests on sandwich specimens under biaxial compressive loading with a universal traction/compression machine (primary load) where the transverse force (secondary load) was applied via two sheaves and a pair of wires with prepressed threaded end fittings. In the case of shear, the deformable square bench applied to sandwich panel is proposed by ASTM standard D8067. The method is used in [21] to assess the core in-plane shear load contribution to failure modes and especially global buckling. The standard is reliable to obtain the in-plane shear properties of sandwich structures with a special focus on

proper hinge mechanisms around the four corners. However, in these two examples, the size of the specimens is closer to that of a panel than a coupon. This shows that multiaxial loading at the coupon scale is difficult due to the small size characteristic of this scale. Thus, an interesting approach is to study the upper stage of the “pyramid of tests” [22] called "technological" – in other words, to switch from coupon scale to panels. This upper scale allows sufficient space to manage boundary conditions (skin reinforcement and ply drops with smooth release) and to add technological elements (local reinforcement, stiffener, etc.) to study their influence on the panel. At this stage of the “pyramid of tests”, we can note the work of [23] in the context of a wind turbine application. A multiaxial test bench is developed enable loading conditions that are representative for realistic loading conditions present in wind turbine blades. A grid-scored foam cored single-curved composite sandwich panel is tested and experimental and computation dialogue is performed via FEM. This state-of-the-art review shows the need to generate wrinkling test cases at the technological scale and to evaluate analytical and numerical models representative of an actual industrial aeronautical application.

Therefore, this paper aims to propose protocols/methods with results and analysis for sandwich panels tested under compressive and shear loading, where wrinkling-type failure is observed. Sandwich panel configurations are chosen to be consistent with the sandwich structures used in light aviation (details in 2.1.2). The VERTEX test bench (Figure 1) developed by Castanié and first used by Serra et al. [24][25] is used here. VERTEX, for “Experimental modelling and validation of composite structures under complex loading” (French acronym) [26], is a French National Research Agency project. It is in line with the need to reduce the number of tests at the coupon scale and to develop more representative testing methods using a virtual testing approach [27]. The VERTEX test bench is based on previous experience

with testing devices using a rectangular box structure [28][29]. The major inspiration comes from the work done by Castanié et al. [30][31], who developed a complex loading test bench where a longitudinal box structure is loaded by four actuators. However, it was pointed out that the area of interest of the test machine was too small (200 x 200 mm^2) and that the effects of boundary conditions were preponderant. Also, it was difficult to estimate the in-plane loads that actually penetrate the test piece. The new VERTEX test bench just keeps the same loading principle and improves these aspects by a larger specimen size and field measurement instrumentation (see §2.2). The level of loading is also about ten times higher. Loading a specimen by a box structure has certain advantages. It allows for the introduction of considerable complex loading (3000 N/mm in tension and compression, 1000 N/mm in shear for the VERTEX test bench) in the specimen by a leverage effect. The operating principle of the VERTEX machine consists of four hydraulic actuators used to load a rectangular box structure (see Figure 1).

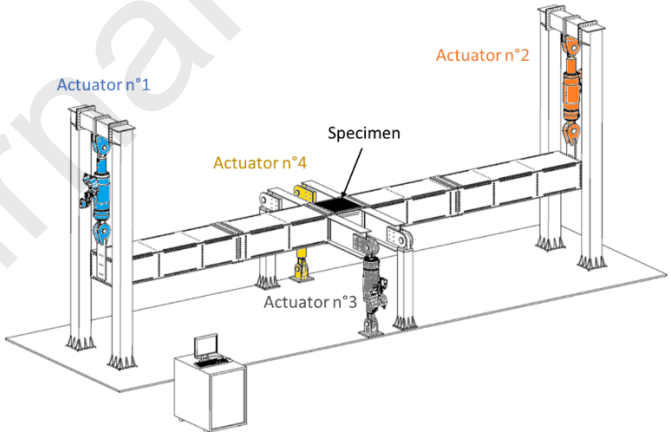

Figure 1: VERTEX test bench.

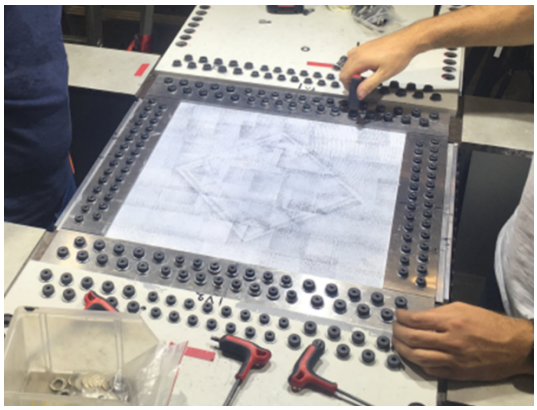

Figure 2: Details of a specimen bolted on to the upper part of the central box of the VERTEX test bench.

The machine structure is a longitudinal box and two cross I-beams. The panel under test is bolted to close the upper part of the central box (see Figure 2). Actuators 1 and 2 can push or pull symmetrically to place the assembly in 4-point bending and, thus, the panel under test is locally loaded in tension or compression. Actuators 3 and 4 can push to twist the centre of the box structure, thus locally loading the tested panel in shear. An air-pressurized rubber bladder system inserted in the box structure between the I-beams allows the specimen to be subjected to an internal pressure of a maximum of 1.6 bar (not used in this experimental analysis). All this was done without using the significant number of powerful, expensive actuators that would have been needed if loading was directly applied to the specimen [32]. Also, the fact that the specimen is an integral component of the test bench structure develops boundary conditions representative of what a sandwich panel can undergo in real conditions (complex loading induced by a structural behaviour, Poisson ratio effect, redundancy of the load paths). Since several studies have used the VERTEX test bench. Serra studied the failure of carbon fibre reinforced polymer notched plates [25][33]. Trellu studied the effect of low-velocity impacts on carbon fibre reinforced polymer plates under multiaxial loading [34].

2 Materials and method

Asymmetric sandwich structures used for helicopter structures [1] inspired the specimen geometry discussed in this paper. The specimens consisted of a monolithic peripheral area and an asymmetric sandwich central area including the tapered region (see Figure 3). The monolithic peripheral area was drilled to bolt the specimen to the VERTEX test bench. The specimen was positioned as shown in Figure 1 and bolted on its 4 sides with 128 screws and aluminium tabs (see

Figure 2). The external dimensions were 558x536 mm², and the sandwich area with the tapered regions was 390x390 mm² and about 21 mm thick (core and skins) (Figure 3). According to the VERTEX methodology described before, the specimens were subjected to a compressive loading or a shear loading through the actuators driven in displacement (Figure 4).

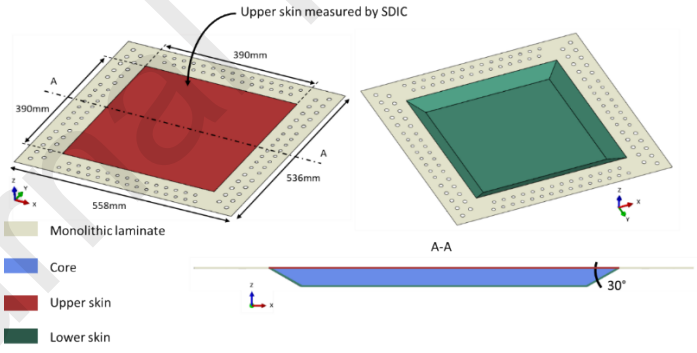

Figure 3: Overall panel geometry.

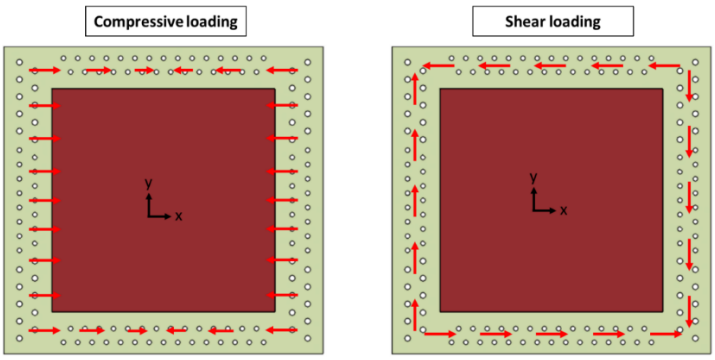

Figure 4: Loads expected to be introduced in the specimens.

2.1 Specimen design

Sandwich structures can potentially fail according to multiple scenarios. The one under study, wrinkling, was selected through rigorous design. Two ways were developed: first, ensure the wrinkling, which must be the first failure scenario to occur in the specimen, then, localise the failure scenario to enable effective observation of the phenomenon and minimise the effect of undesired boundary conditions, as far as possible.

2.1.1 Geometry

The lower skin of the sandwich plane is not accessible as it faces the interior of the test bench box structure.

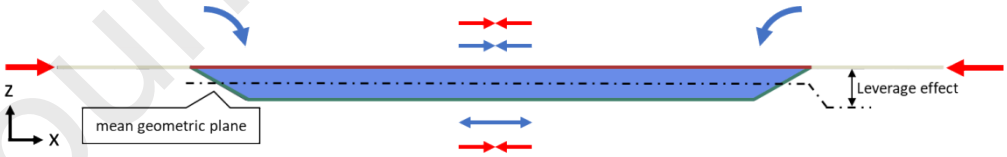

Figure 5: Bending effect on asymmetric sandwich structure.

Since the observable surface is the upper skin, it is imperative to localise the wrinkling on it. In compression, the asymmetric geometry of the plate allows the upper skin to be more loaded than the lower skin and therefore to buckle locally first. This offset between the load introduction axis and the mean geometric plane of the sandwich structure leads to a bending

moment, which induces an additional compressive load in the upper skin and a tensile load in the lower skin (blue arrows in Figure 5). This phenomenon has already been identified with asymmetric sandwich structures tested by Castanié et al. [31] and recalled in [1]. Under shear loading, the offset of the middle plane does not play any role because the tension and compression at 45° cancel each other out. The shear load is shared in the same proportion as the skin stiffness [31]. Therefore, reinforcement in the lower skin is required to localise the buckling on the upper skin (Table 1).

2.1.2 Materials

Pre-sizing using finite element models and the experience acquired during previous compression tests on sandwich beams helped to define the choice of materials, stacking sequences, reinforcements, and core thickness allowing wrinkling to be obtained as the first failure scenario under compressive and/or shear load. The materials used for the specimens were a PMI foam of 51 kg/m^3 or NOMEX® honeycomb of 29 kg/ m^3 and prepreg epoxy/carbon woven fabric that was unidirectional for the skin (Table 1). Despite lower strengths and stiffnesses than the Nomex honeycombs, foams remain widely used in light aviation due to the ease of manufacturing (cutting, machining, forming, and bonding to the skins). The skins were glued to the core by an adhesive film. A "one-shot/co-cured" process was used in the autoclave. To have the upper skin as flat as possible, it faced the mould and calibrated plies were used to leave the core undeformed with the ply drops (Figure 6). No counter-mould was used; a vacuum bag was applied instead. The core (foam or honeycomb) was 20 mm thick.

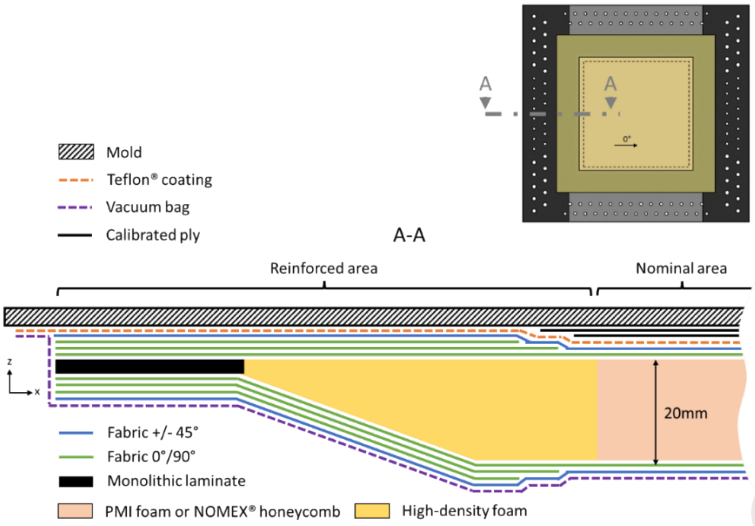

Figure 6: Cross-sectional drawing of specimens with the manufacturing process.

To localise the wrinkling in the centre of the panel, a high-density foam frame was used to reinforce the tapered area of the sandwich where local stresses could be relatively high (Figure 7). For specimens under compressive loads, the nominal area was 260x260 mm^2 (pink in Figure 7(a)). For specimens under shear load, the nominal area (pink in Figure 7(b)) was lozenge-shaped so as to have edges perpendicular to the main stresses at 45°. Pre-sizing had shown that buckling occurred at the corners and was restrained if a square reinforcement shape was used, which was not intended. For specimens with NOMEX® honeycomb core, the ribbon direction (L) is specified in Figure 7.

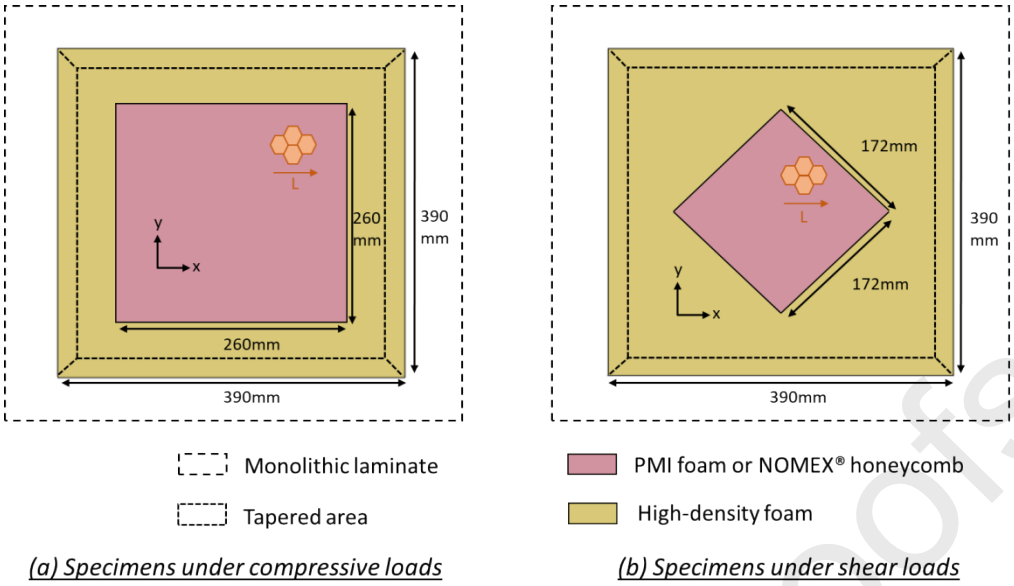

(a) Specimens under compressive loads

(b) Specimens under shear loads

Figure 7: Definition of the cores of the specimens.

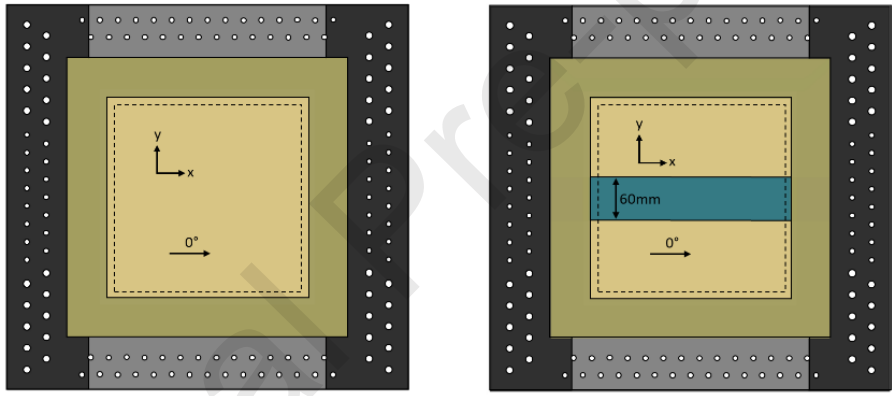

(a) Specimens F51_D1 and N29_D1 under compressive loads

(b) Specimens F51_D2 under compressive loads

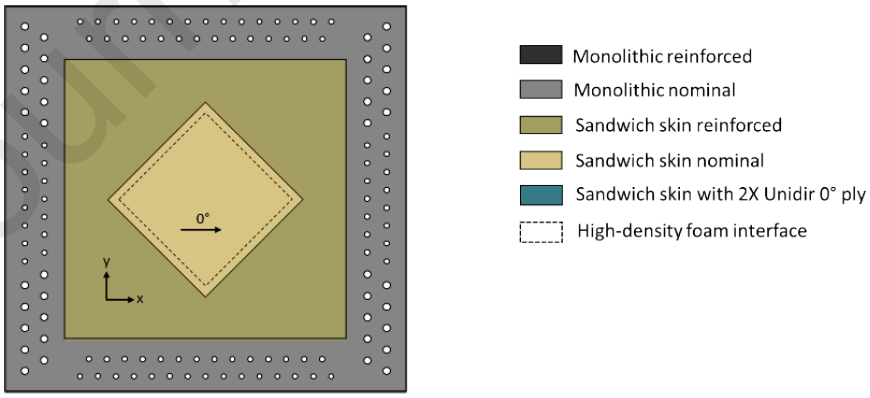

(c) Specimens F51_D3 and N29_D3 under shear loads

Figure 8: Definition of the specimen skins.

For the same reasons, skins in the tapered area were reinforced (dark brown area in Figure 8). For specimens under compressive load, the monolithic area was reinforced in the specimen height (dark area in Figure 8(a) and (b)), to avoid bolt bearing. In the width, the monolithic area was left with a relatively thin laminate (grey area in 8(a) and (b)) so that this area did not bear all the loads at the expense of the sandwich area. For specimens under shear load, the nominal skin (light brown area in Figure 8(c)) was lozenge-shaped. It should be noted that ply drops are not detailed in Figure 8; in the sandwich area, 10 mm was left between each ply drop. The nominal skin (light brown area in Figure 8) extended beyond the nominal core area (pink area in Figure 7), to avoid having a ply drop and core interface in the same area. The area where the stacking sequence corresponds to Table 1 is called the "nominal area" (where wrinkling is expected) and is shown in Figure 6.

In the nominal area, the panel configurations tested were consistent with the sandwich structures used in light aviation. Five specimens were manufactured, which corresponded to typical stackings used in different locations of the aircraft. In specimen F51_D2, tested under compressive load, a 60 mm wide strip of 2 x unidir 0° ply was added (blue area in Figure 8(b)). In specimen N29_D3, tested under shear load, the ribbon direction, L, of the honeycomb core was on the x-axis (Figure 7(b)) and not at the 45° direction of the theoretical principal stresses.

Table 1: Specimens stacking sequence in nominal area. Specimen nomenclature is F51_... or N29_... for PMI foam or NOMEX® honeycomb respectively and ..._Dx for specified stacking sequence.

Specimen	**F51_D1**	**N29_D1**	**F51_D2**	**F51_D3**	**N29_D3**
Loading	**Compressive**	**Compressive**	**Compressive**	**Shear**	**Shear**
Stacking sequence	Fabric +/- 45°	Fabric +/- 45°	Fabric +/- 45°	Fabric +/- 45°	Fabric +/- 45°
			2 x Unidir 0°		
	Fabric 0°/90°	Fabric 0°/90°	Fabric 0°/90°	Fabric +/- 45°	Fabric +/- 45°
	adhesive film	adhesive film	adhesive film	adhesive film	adhesive film
	PMI foam	NOMEX® honeycomb	PMI foam	PMI foam	NOMEX® honeycomb

	adhesive film	adhesive film	adhesive film	adhesive film	adhesive film
	Fabric 0°/90°	Fabric 0°/90°	Fabric 0°/90°	Fabric +/- 45°	Fabric +/- 45°
	Fabric +/- 45°	Fabric +/- 45°	Fabric +/- 45°	Fabric +/- 45°	Fabric +/- 45°
				Fabric +/- 45°	Fabric +/- 45°

2.2 Measurement systems

Because of intrinsic structural redundancies in the VERTEX test bench and the fact that the specimen is an integral component of the test bench structure, no transfer function currently links actuator forces with stresses entering the specimen. To estimate the stresses entering the specimen during the test, an in-situ strain measurement method had to be used. To capture the failure scenario, the test bench was equipped with several measurement systems as shown in Figure 9.

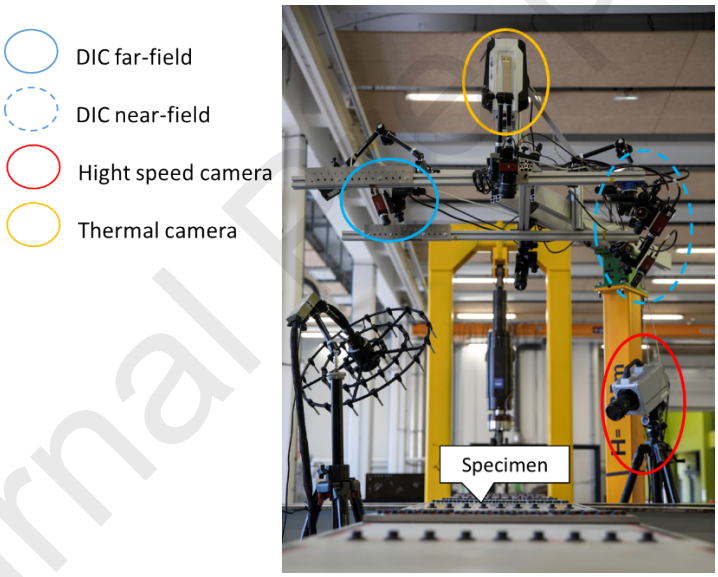

Figure 9: Camera set up on the VERTEX test bench.

Stereo Digital Image Correlation (SDIC) is a very reliable method that has already been used on previous VERTEX tests [24][25][34]. Moreover, SDIC can measure out-of-plane displacements and reconstruct a 3D shape evolution. This is particularly useful for observing wrinkling, which manifests itself as short, out-of-plane waves in the skins. To achieve this SDIC, a speckled pattern was applied to the specimen's upper skin. It was made by using paint rollers

where the size of the dots was chosen according to the cameras' resolutions and fields of view. Two SDIC systems of five Mpx cameras were employed. A far-field system measured the entire upper surface of the specimen up to the tabs (area of 400x400 mm) (Figure 10(b)). This allowed the overall displacement fields in the specimen to be analysed. A near-field system focused on a particular, limited area of the specimen (Figure 10(a)), thus improving the accuracy of measurement. The focus was chosen where wrinkling was likely to occur. The acquisition frequency was set to two images per second. Vic3D_ software (Correlated Solutions Inc., Columbia, SC, USA) was used for post-processing.

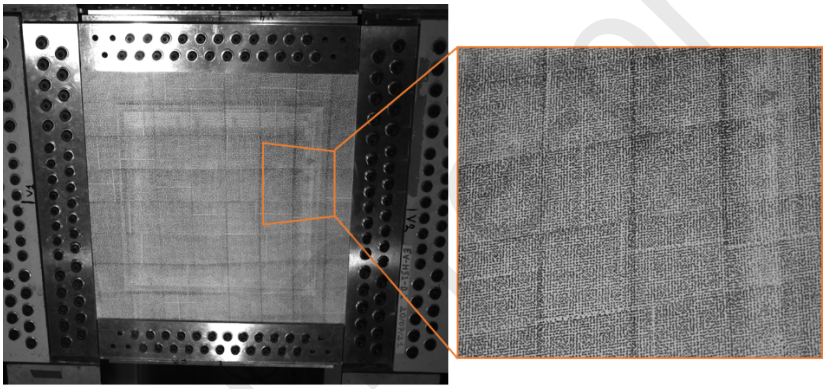

(a) SDIC far-field capture (b) SDIC near-field capture

Figure 10: SDIC captures.

A high-speed camera (7000 fps) was also used to observe a potential explosive failure (Figure 11(a)). Finally, an infrared camera (500 fps) was added to the setup (Figure 11(b)) to allow for possible wrinkling-type failure measurements. In particular, it enables the capture of fiber breakages and their locations, thus permitting the identification of the failure scenario. In the lower skin, several “Rosette” gauges were used (Figure 12). An acoustic camera was also present for one trial (Figure 9, left side) but the results were not sufficiently relevant and are not reported here.

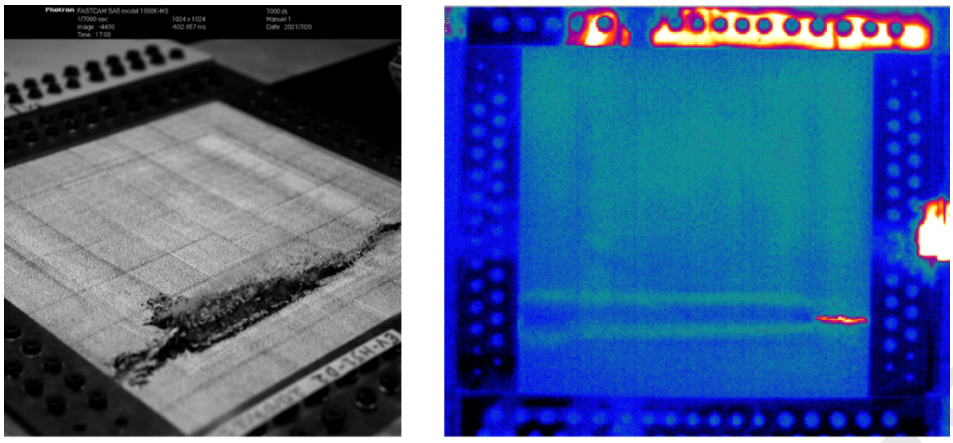

(a) Fast camera capture (b) Infrared camera capture

Figure 11: High-speed camera and infrared camera captures.

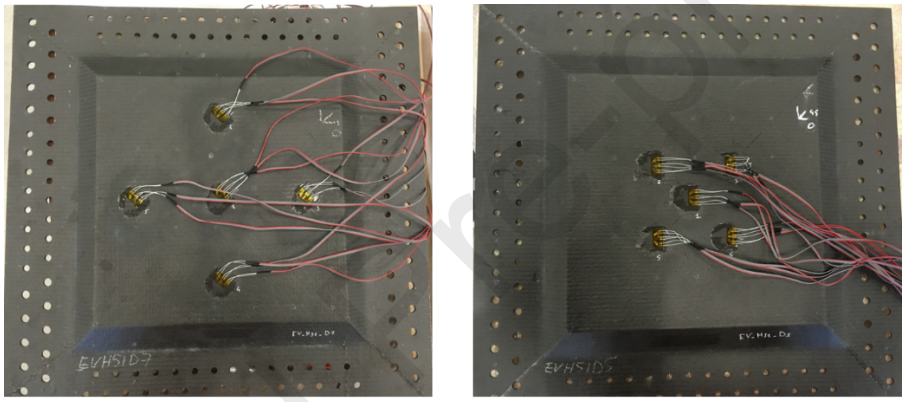

(a) "Rosette" gauges in lower skin of specimens tested under compression (b) "Rosette" gauges in lower skin of specimens tested under shear

Figure 12: Locations of "Rosette" gauges.

3 Results

Installing the specimen on the test bench by bolting the 128 screws induced some initial stresses in it as the sandwich panel had high bending stiffness and did not compensate for the initial geometrical imperfections between the test bench and the specimen. Installation of the specimen on the test bench thus yielded residual compressive and shear strains. F51_D3 was the specimen where the highest residual principal compressive strains, of about -500 µstrains,

were observed in the nominal area, i.e. 10% of the ultimate failure strain. However, an average of -200 µstrains in the nominal area was observed over all specimens.

3.1 Overall behaviour

3.1.1 Specimens under compression

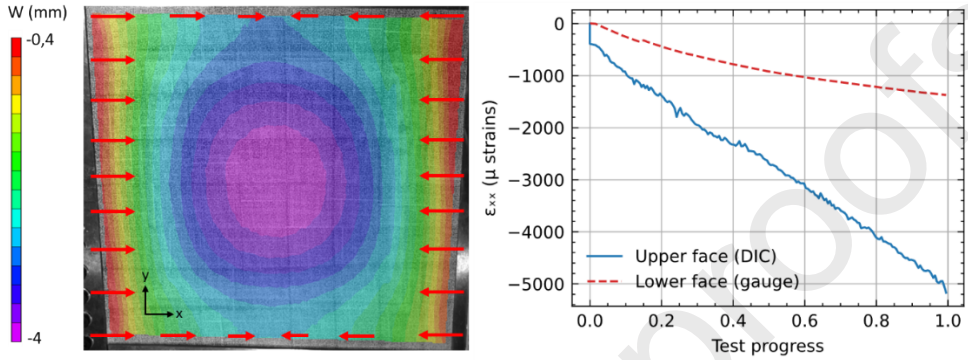

(a) Out of plane displacement field of the upper face just before failure.

(b) ε_{xx} of upper and lower faces against test progress.

Figure 13: Specimen F51_D1 general behaviour.

The specimen panels bent globally (Figure 13(a)), a consequence of the asymmetric geometry (see § 2.1.1). The plot of Figure 13(b) shows the evolution of $\boldsymbol{\varepsilon_{xx}}$ at the centre of both skins and highlights the non-linear bending behaviour of the tested panel. The upper skin had a quasi-linear response and underwent higher loading whereas the response of the lower skin was non-linear. The nonlinearity was due to coupling of the sandwich deflection and the load. This behaviour had already been observed with asymmetric sandwich panels tested by Castanié et al. [31] and was expected.

3.1.2 Specimens under shear

The global bending behaviour presented previously was not present here because the tension and compression at 45° cancelled each other out. The plot of the strain evolution at +/-45 ($\boldsymbol{\varepsilon_{xy}}$) shows a quasi-linear response in both skins. Nonlinearity was not likely to occur as the deflection was very small. Note that strains were greater in the upper face, as a consequence

of the stiffness difference between the sandwich skins: the upper skin had two plies of +/-45° fabric, whereas the lower had three plies of +/-45° (Table 1). This confirms the pre-sizing performed.

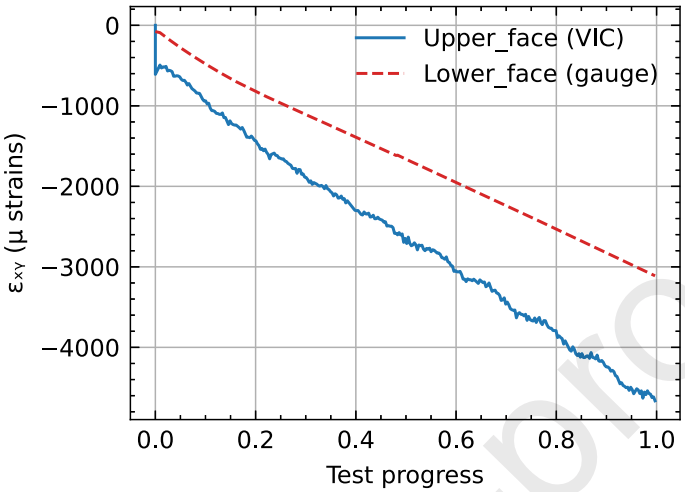

Figure 14: Specimen F51_D3 $\boldsymbol{\varepsilon_{xy}}$ of upper and lower faces against test progress.

3.1.3 Strain fields

Figure 15 shows in-plane strain fields in the upper face obtained by SDIC of two specimens just before failure. The reference image (time 0 and strain field equal to zero) was taken when the specimen was simply laid down on the VERTEX bench, i.e. before it was clamped by bolting the 128 screws. In the nominal area, strains were globally uniform and corresponded to the theory. For the specimens under compressive loading, the average principal compressive strain direction in the nominal area was not more than 5° from the x-axis. Some transverse traction appeared (Figure 15 positive $\boldsymbol{\varepsilon_{yy}}$ field of F51_D1 column). The specimen was clamped on its 4 sides and reacted with the boundary condition imposed by the central box of the VERTEX test bench. Poisson's strains were thus blocked and transverse tension appeared in consequence. This must be quite representative of what a sandwich panel can undergo in a structure in real conditions. Some shear was observed at the corners, but it was nearly zero in

the nominal area (Figure 15 $\boldsymbol{\varepsilon_{xy}}$ field of F51_D1 column). For the specimens under shear loading, the average principal compressive strain direction was about 38° from the x-axis. Some traction is shown by the non-null $\boldsymbol{\varepsilon_{xx}}$ components (Figure 15 positive $\boldsymbol{\varepsilon_{xx}}$ field of F51_D3 column). This was a consequence of a coupling between torsion and bending of the of the box structure. When operated for this stress, it generated parasitic tensile forces. This has already been encountered in [34] [30]. For these tests, compensation was not carried out to diminish these tension forces since the authors were afraid of perturbing the wrinkling phenomena. Local gradients, in the form of strips (Figure 15 $\boldsymbol{\varepsilon_{xx}}$ field of F51_D1 column and $\boldsymbol{\varepsilon_{xy}}$ field of F51_D3 column) were present at the edge of the nominal area, reflecting a local bending induced by wrinkles. The strain fields exhibited a grained noise, a consequence of the SDIC parameters used, which are justified in § 3.2.1.

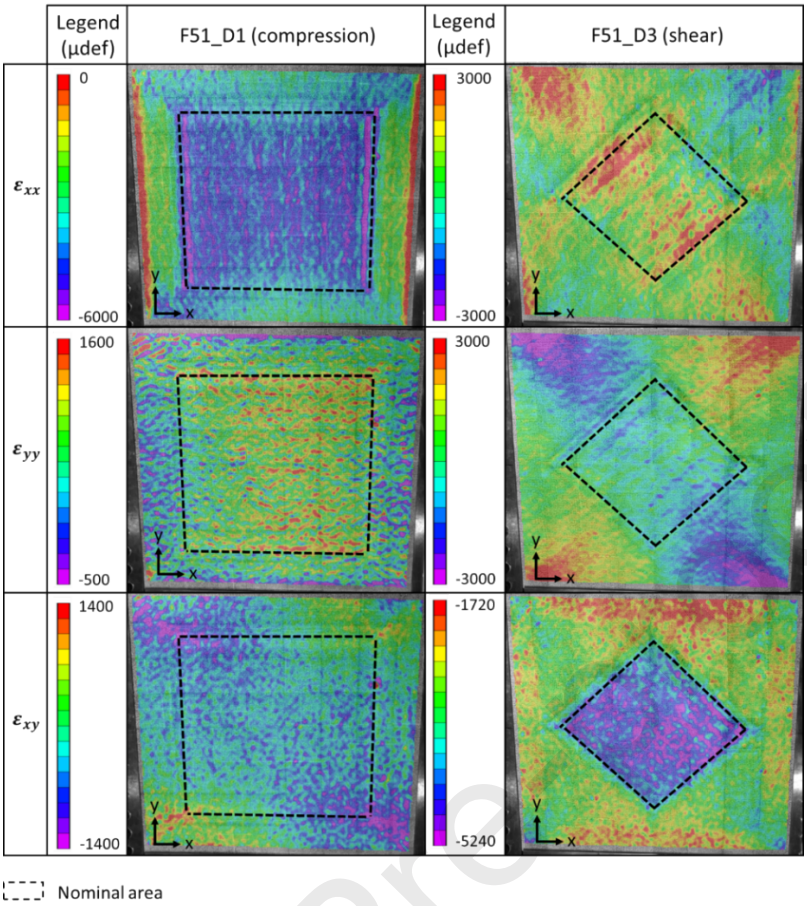

Figure 15: Strain fields just before failure of the upper faces of specimen F51_D1 under compressive loading and specimen F51_D3 under shear loading.

3.2 Local behaviour

3.2.1 Specimens under compression

3.2.1.1 Buckling behaviour

Locally, specimens F51_D1 and F51_D2, presented similar behaviour. The formation of a wrinkling at the interface between the nominal core and the high-density foam can be observed in Figure 16(a) and (b), and Figure 18(a) and (b). It appears at the end (>80%) of the test (Figure 16(b) and Figure 18(b)). The failure load (test progress equal to 1) is the moment when the core breaks in tension (see the following subsection 3.2.1.2) and the plate loses its

stiffness. a very loud noise is heard which also corresponds to the sudden propagation of a crack in the skin at the local buckling level.

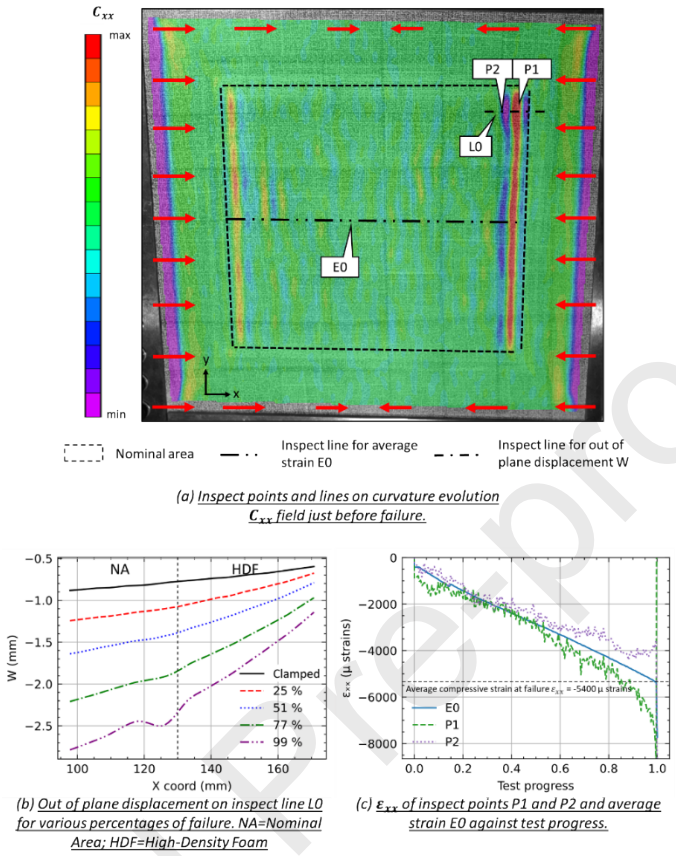

(a) Inspect points and lines on curvature evolution C_{xx} field just before failure.

(b) Out of plane displacement on inspect line L0 for various percentages of failure. NA=Nominal Area; HDF=High-Density Foam

(c) ε_{xx} of inspect points P1 and P2 and average strain E0 against test progress.

Figure 16: Specimen F51_D1 local behaviour.

Wrinkling failure localisation is driven by geometrical and mechanical aspects. The nominal/high-density core interface leads to a gap in core stiffness (high-density core modulus is about three times higher than the nominal PMI foam) and induces local bending in the sandwich skins [35][36] likely to trigger instabilities. Moreover, SDIC revealed an initial slight local dent in this area in specimens tested under compression (Figure 17). The dent was about 0.04 mm, which is about 10% of the sandwich skin thickness in the nominal area.

A technical explanation is difficult to justify, especially since particular attention was paid to the flatness of the upper skin (see § 2.1.2 and Figure 6). It was probably a manufacturing defect. As for dents in compression after impact on sandwiches [37][38], this shape generates

non-linear local bending moments which may increase the depth of the dent and therefore promote the local appearance of wrinkling [19]. So, this local imperfection localises the wrinkling failure in the specimen. Figure 16(c) and Figure 18(c) show plots of the strain's $\boldsymbol{\varepsilon_{xx}}$ evolution measured at inspection points P1 and P2, and the averaged strain E0 taken along a line in the centre of the nominal area (see Figure 16(a)). The average strain is calculated via the ratio of the difference between the two ends of the line E0 with the length of the line E0 (as a numerical extensometer). The evolutions of strain in P1 and P2 differ from the averaged E0. This is due to the non-linear local response initiated by the dent, which generates out-of-plane displacements and thus affects local in-plane strains. Strain evolution at P1 and P2 first decreases linearly with the load, then becomes non-linear as a consequence of the appearance of the wrinkling wave (around 80% of the failure load). This phenomenon was local, so the non-linearity did not influence the average strain E0, which remained linear until failure. In specimen F51_D2, where a 60 mm wide strip of two Unidir 0° plies was added, the wrinkling was positioned in this stiffened area, which drained the loads (Figure 18 (a)). The localisation of wrinkling failure can thus be chosen by playing locally on the in-plane stiffness of the skin.

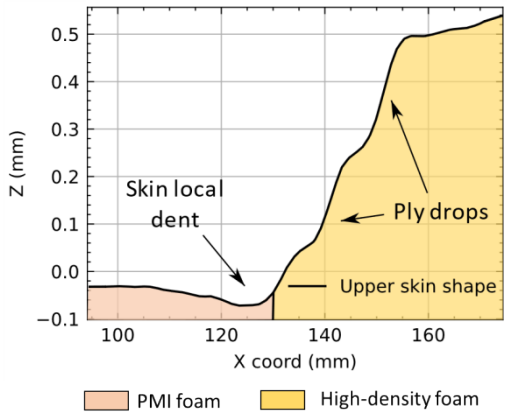

Figure 17: Upper skin initial shapes against X coordinate at nominal and high-density foam interface of specimen F51_D1.

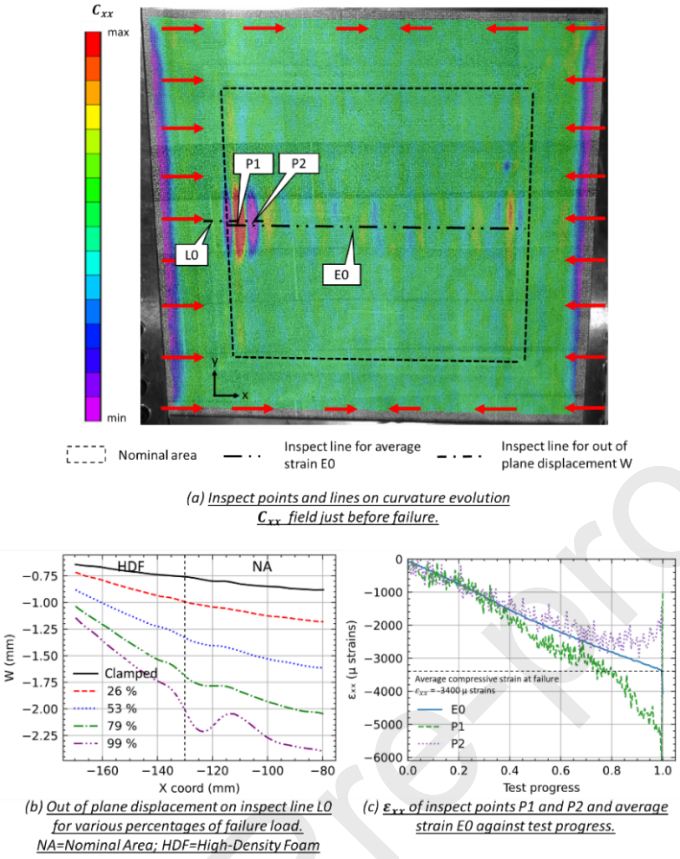

(a) Inspect points and lines on curvature evolution C_{xx} field just before failure.

(b) Out of plane displacement on inspect line L0 for various percentages of failure load. NA=Nominal Area; HDF=High-Density Foam

(c) ε_{xx} of inspect points P1 and P2 and average strain E0 against test progress.

Figure 18: Specimen F51_D2 local behaviour.

Noises in the strain curves at P1 and P2 are observed in Figure 16(c) and Figure 18(c). Local strain computation from DIC depends on several parameters. The displacement is averaged over a square of size $J(pixels) = N_{step}(N_{filter} - 1) + N_{subset}$, where N_{subset} is the size of the area used to track the displacement between images, N_{step} is the number of pixels between the points that are analysed during correlation and N_{filter} is the number of points in the calculation window (see Figure 19). The decay filter used is a 90% centre-weighted Gaussian filter. A good compromise was chosen between data noise and sufficient accuracy to capture the actual strain at the centre of the buckling wave. The wrinkling half wave-lengths observed were about 10 mm. A strain calculation window of 45 pixel square was chosen to have the same order (pixel size is equal to 0.2 mm). With these parameters, the average confidence

margin for out-of-plane displacement W is about 0.003 mm. In Figure 16(a) and Figure 18(a) the curvature evolution $\boldsymbol{C_{xx}}$, calculated as the inverse diameter of the circle locally tangent to the out of plane displacement, does not have a quantitative legend. Quantitative results are not consistent with the expected order of magnitude. As a strain computation, the curvature depends on a calculation window that is far too large compared to the one required to obtain consistent data in the local wrinkle area. However, the curvature evolution gradient remains an intersecting indicator for locating wrinkling. These remarks are valid for specimens under shear.

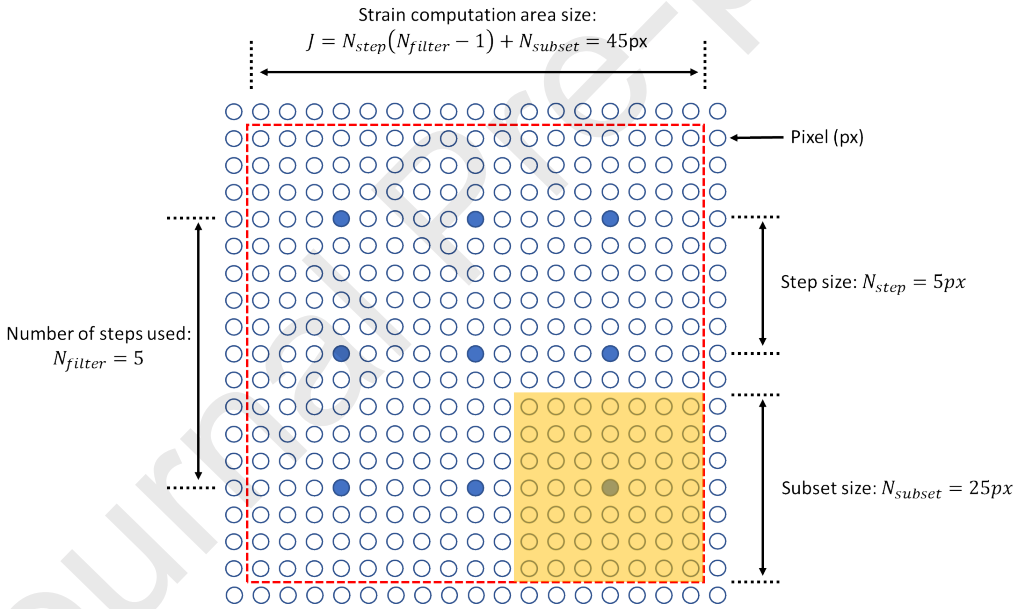

Figure 19: Parameters of the local strain computation from SDIC (scheme symbols not representative of the values used in this paper) [33], [34].

3.2.1.2 Failure scenario for compression loading

For specimens F51_D1 and F51_D2, the failure behaviour was similar. The specimens failed by wrinkling of the upper skin, which validates the design of the specimens. A wrinkling wave

appeared, the core was crushed, and the wave then spread over the width. Finally, the core failed in tension and the wave moved on over a large part of the nominal area (Figure 20).

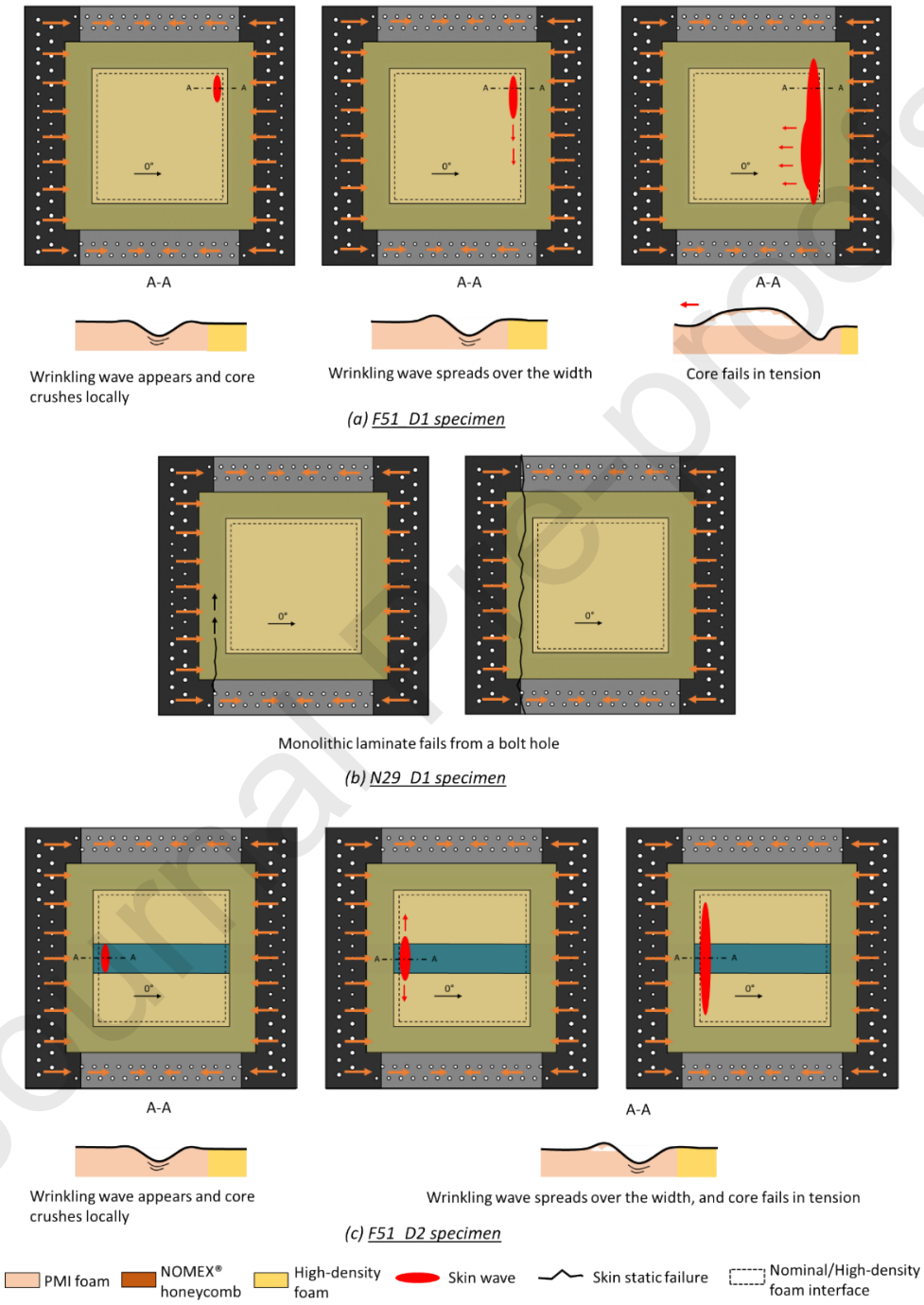

Figure 20: Failure scenario for specimens under compression.

The wrinkling wave appearance lasted a few seconds and could be observed by SDIC (acquisition frequency of 2 fps). However, failure, beginning with core crushing, was very fast and lasted about 2 milliseconds. The failure scenarios could be accurately reconstructed thanks to images taken by the high-speed camera (Figure 21). Skin static failure could be observed soon after the wrinkling failure (Figure 21). An exception, specimen N29_D1, failed by a static compressive rupture in the monolithic laminate area (Figure 20(b)). Thanks to the thermal camera, we observed that the failure propagated from a hole at the edge of the specimen panel. That area presented stress concentrations where ply drops accumulated. It seems that the upper skin in the nominal area did not reach the wrinkling critical stress. However, it allowed a minorant to be found for comparison with other specimens (see § 3.3).

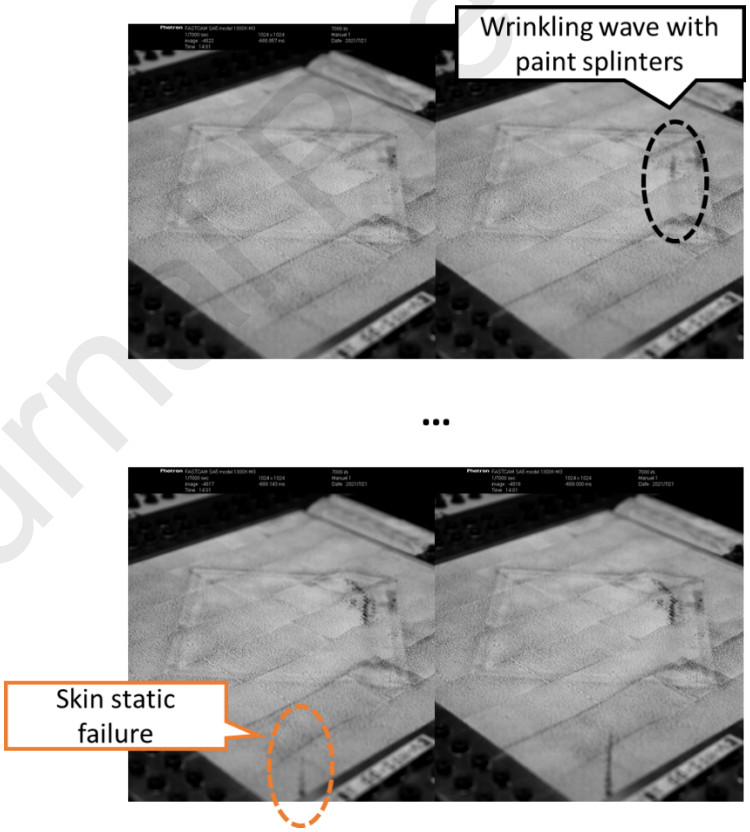

Figure 21: Images taken with a high-speed camera (7000 fps) for specimen F51_D3 tested under shear.

The specimens were cut postmortem, and the foam crushing and tensile cracks were distinct in specimens with foam core (Figure 22).

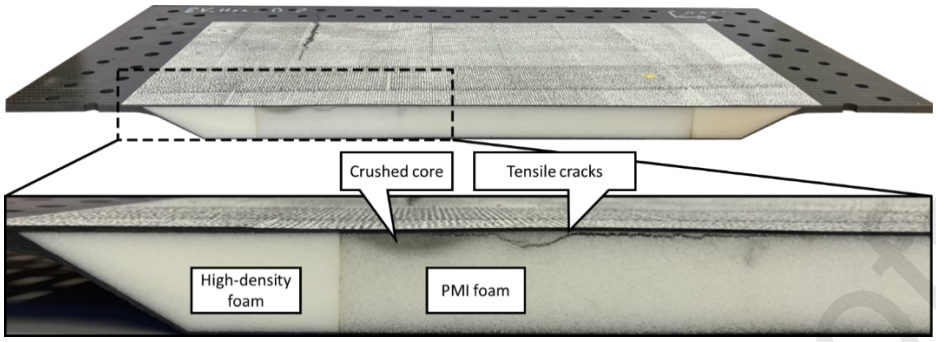

Figure 22: Post-mortem cutting of specimen F51_D2.

3.2.2 Specimens under shear

3.2.2.1 Buckling behaviour

Contrary to the situation in specimens under compressive loading, the formation of several wrinkles was observed in the nominal area. For specimen F51_D3, the maximum wave amplitude appeared at the interface between the nominal area and the high-density foam (Figure 23(a) and (b)). Specimen N29_D3 showed interesting behaviour. The maximum wave amplitude was located in the central nominal area (Figure 24(a) and (b)). The wrinkling wave was not precisely at -45° from the x-axis but around -40° (Figure 24(a)), practically perpendicular to the principal compression strain (see Table 2). This is consistent with predictions by several authors who have worked on the theory of wrinkling under combined loading [39] [40]. We did not observe it in specimen F51_D3 because the wrinkling wave direction is driven by the interface with high-density foam, which was precisely at -45° from the x-axis.

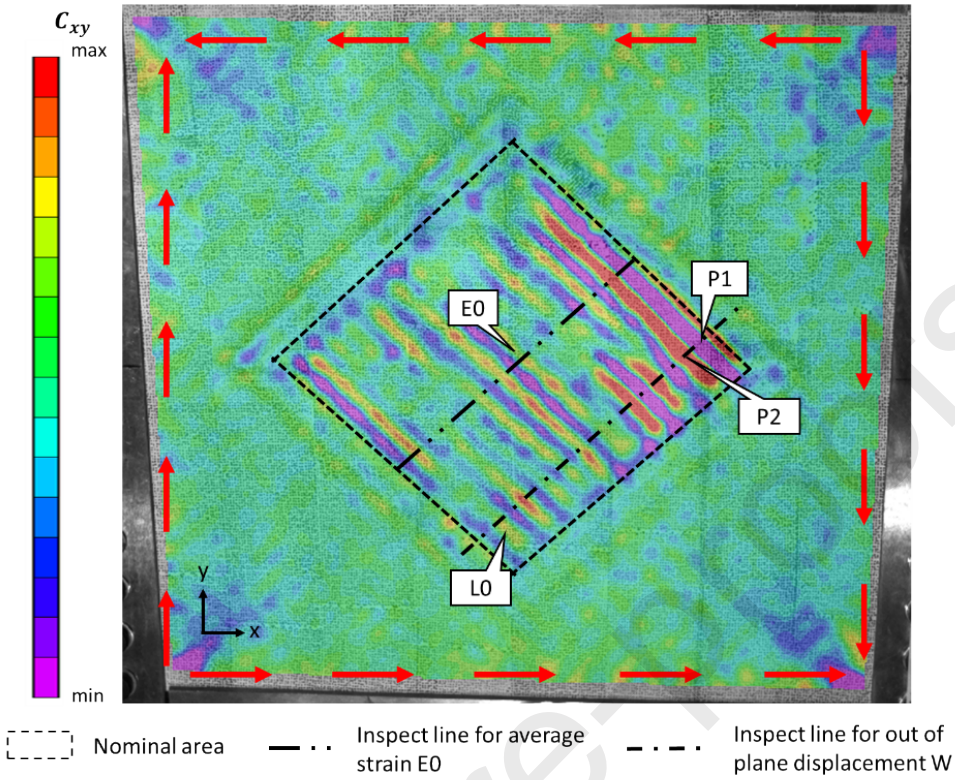

(a) Inspect points and lines on curvature evolution C_{xy} field just before failure.

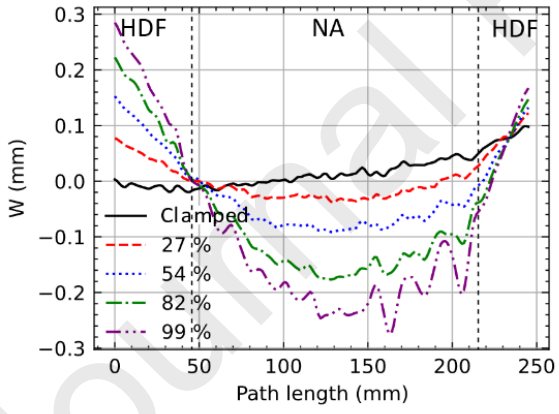

(b) Out of plane displacement on inspect line L0 for various percentages of failure load. NA=Nominal Area; HDF=High-Density Foam

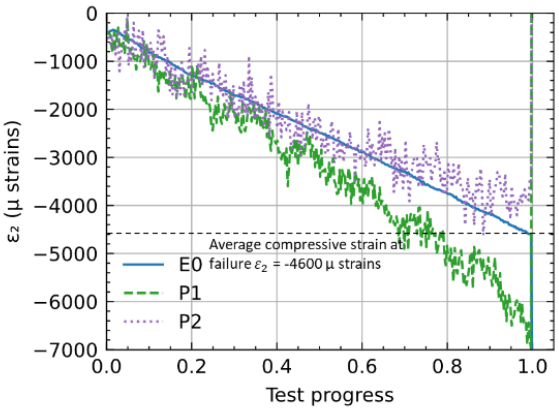

(c) ε_2 compressive principal strain for inspect points P1, P2 and average strain E0 test progress.

Figure 23: Specimen F51_D3 local behaviour.

The rigid motion of the panel has been removed, leaving only deformation components of displacement, shown in Figure 23 (b) and Figure 24 (b). The processing method, directly proposed by the software, calculates the average transformation for each image and inverts it to obtain an image with an average displacement/rotation of zero [41]. Only object

deformation will be reflected in the transformed U, V, and W displacements. The process is used for visualization purposes. For this loading case, an inherent behaviour of the test bench makes the overall rigid out-of-plane displacement of the panel very great relative to its deflection and even more so to the buckling waves.

Similarly to what was observed in the compressive test, the evolution of the principal compressive strains $\boldsymbol{\varepsilon_2}$ at inspection points P1 and P2 (Figure 23(c) and Figure 24(c)) showed a linear trend with load, followed by a non-linear regime at the end. Again, this can be attributed to the onset of local buckling that took place at around 80% of the failure load. We note that, for specimen N29_D3, the strain evolution at P1 and P2 (slope of the curve) was similar to that of the averaged strain E0 taken in a line in the centre of the nominal area (Figure 24(c)). No initial imperfection was observed in this area. The analysis proposed in §3.2.1.1, where an initial defect affected in-plane strains, was not accurate here. We observed a wave phenomenon in curves P1 and P2 (Figure 24(c)). This was not considered as true mechanical behaviour but as an artefact of the SDIC strain calculation process, which could be due to the frequency of the lighting in the test room.

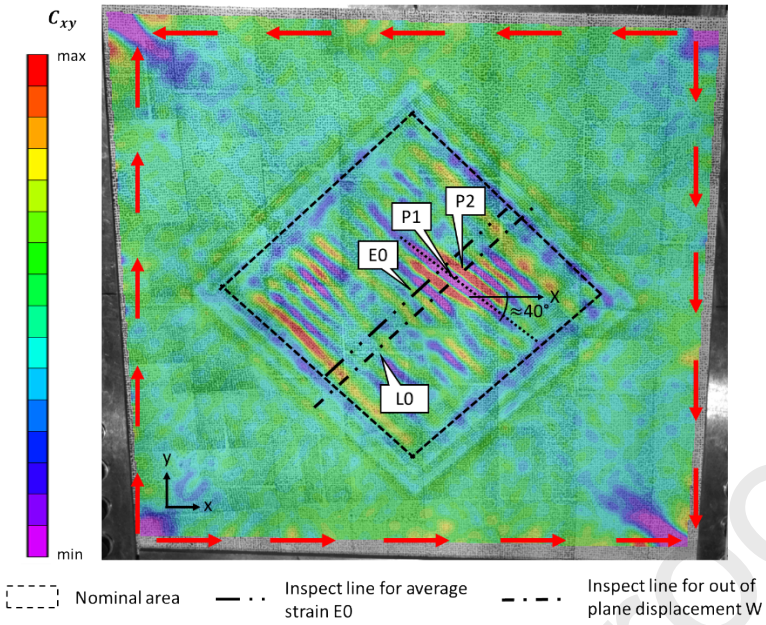

(a) Inspect points and lines on curvature evolution C_{xy} field just before failure.

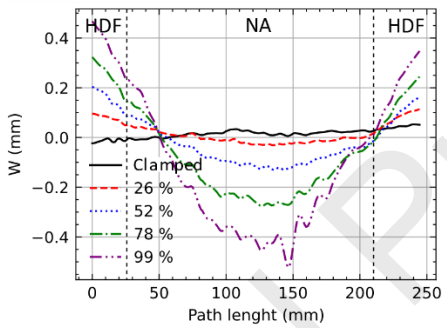

(b) Out of plane displacement on inspect line L0 for various percentage of failure load. NA=Nominal Area; HDF=High-Density Foam

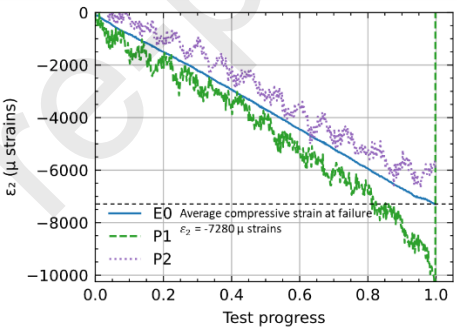

(c) ε_2 compressive principal strain for inspect points P1, P2 and average strain E0 against test progress.

Figure 24: Specimen N29_D3 local behaviour.

3.2.2.2 Failure scenario for shear loading.

For specimens under shear, the wrinkles appeared around the direction -45° from the x-axis because the compression along the +45° direction was associated with shear loading (Figure 25). Then, the scenario was comparable to those observed in specimens under compression. Skin static failure could be observed soon after the wrinkling failure.

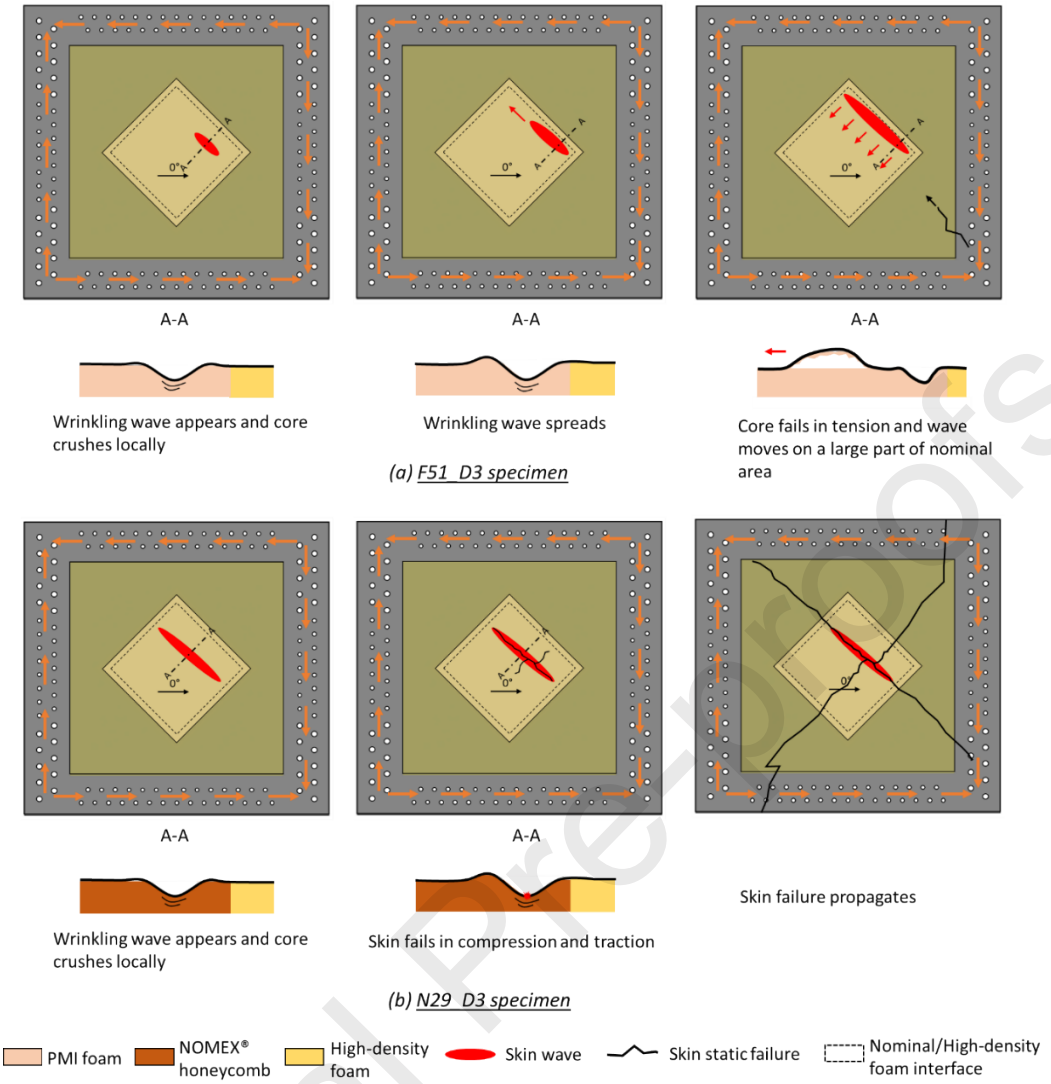

Figure 25: Failure scenario for specimen under shear.

3.3 Compressive and shear strains at failure

Table 2: Average strain at failure.

Specimen	**F51_D1**	**N29_D1**	**F51_D2**	**F51_D3**	**N29_D3**
Loading	Compression	Compression	Compression	Shear	Shear
Failure type	wrinkling	Compressive Skin static failure	wrinkling	wrinkling	wrinkling
Principal compressive direction	3.9°	3.0°	3.6°	38.2°	38.5°
Average compressive strain at failure	ε_{xx} = -5400 µstrains	ε_{xx} = -6050 µstrains	ε_{xx} = -3400 µstrains	ε_2 = -4600 µstrains	ε_2 = -7280 µstrains

Noting the strain where the failure occurs as the actual wrinkling strain might be interesting. However, in this area, the wrinkles appear, and the stress state is no longer in the membrane only but also in bending; making the measurement and calculation of an equivalent pure membrane stress complex. From an engineer's point of view, to find a wrinkling's allowable, it is more appropriate and conservative to take the average strain in the nominal area; which remains linear throughout the test (see §3.2).

Table 2 shows the superiority of the NOMEX® honeycomb core (29 kg/m^3, noted N29) over the PMI foam core (51 kg/m^3, noted F51) in wrinkling resistance – both in compression (where the specimen N29_D1 even failed statically) and in shear. Such a result is logical because the out-of-plane characteristics are superior at almost twice as high as the PMI foam. The superiority is even more important if we relate them to the mass. The specimen F51_D2 shows that the concentration of stiffness in a local area (60 mm strip of 2 × 0° ply) drains the loads, localises the buckling and causes the sandwich structure to wrinkle at a lower strain level. Note that a quantitative comparison between specimens F51_D1 and F51_D2 is not possible because their overall membrane stiffness is not the same.

4 Conclusion

This paper presents an experimental methodology to test the wrinkling behaviour of aeronautic sandwich structures. Five sandwich panels were bolted on 4 sides and tested in compression and shear using the VERTEX test bench. The technological/panel scale with the VERTEX test bench allows multiaxial loading and boundary conditions that come close to the reality of what a sandwich panel can undergo in an aeronautical lightweight structure. The specimen geometry, material definition and measurement tools have demonstrated their effectiveness in the observation of wrinkling. The asymmetric geometry of the sandwich

specimens with core and skin reinforcements allows the wrinkling failure to be located in the upper skin while reducing side effects. Locally, specimens (except N29_D1 which failed statically) present similar failure behaviour. One or more wrinkles appear at around 80% of the failure load. The specimen then fails locally by core crushing, which is quickly followed by a core tensile failure and wave spreading over a large area. This scenario lasts about 2 milliseconds and was successfully observed with a high-speed camera (7000 fps). It appears that wrinkling is driven by mechanical and geometrical aspects. The interface between the high-density foam and nominal area induces a gap in out-of-plane core stiffness (high-density core modulus is about three times higher than the nominal PMI foam), where initial geometrical defects are also observed in some specimens. These aspects develop local bending and displacements with load, giving rise to both in-plane and out-of-plane stress. This facilitates the start of the buckling process and localises the wrinkling failure. 3D shapes and strain field evolutions have been quantified thanks to SDIC. In-plane strains in the wrinkling area show the onset of local buckling. Compressive strains first decrease linearly with load, until the wrinkling wave appears. It then becomes non-linear, a consequence of local bending due to the wrinkling wave. In the specimen N29_D3, tested under shear load, wrinkles were observed in the centre of the panel. The wave's direction was practically perpendicular to the main compression strain, which is consistent with theory. Panel scale permits the addition of technological elements such as in specimen F51_D2, where a strip of carbon prepreg Unidir 0° ply was added in the sandwich upper skin, as is typical of some sandwich structures used in light-weight aviation. The stiffer area drains the loads, localises the buckling and causes the sandwich structure to wrinkle at a lower strain level. Comparison between specimens with PMI foam (51 kg/m^3) core and specimens with NOMEX® honeycomb (29 kg/m^3) shows the superiority of honeycomb core in wrinkling-type failure resistance. This result is logical

because, even though the honeycomb has a lower density than the foam, its out-of-plane mechanical properties are higher.

These tests at the technological scale provide a large amount of interesting data on wrinkling phenomena. The next step is the computation/testing dialogue with existing analytical and advanced non-linear finite element models. This is intended to evaluate models in an actual industrial aeronautical application and will be the object of a forthcoming paper.

Acknowledgements

This research is part of PhD thesis CIFRE in collaboration with the aircraft manufacturer Elixir Aircraft (https://elixir-aircraft.com). This work was partially funded by the "Fondation Jean-Jacques et Felicia Lopez-Loreta pour l'Excellence Académique" as part of the VIRTUOSE (VIRTual testing of aerOnautical StructurEs) project (https://websites.isae-supaero.fr/virtuose/). The authors gratefully acknowledge CALMIP (CALcul en MidiPyrénées, (https://calmip.univ-toulouse.fr) for access to the HPC resources and allows fast and effective computations. The authors would also like to thank C3Technologies (http://www.c3technologies.fr) for their qualitative manufacture of the sandwich specimens.

Declaration of conflicting interests

The author(s) declared no potential conflicts of interest with respect to the research, authorship, and/or publication of this article.

References

[1] Castanié B, Bouvet C, Ginot M. Review of composite sandwich structure in aeronautic applications. Compos Part C Open Access 2020;1:100004. https://doi.org/10.1016/j.jcomc.2020.100004.

[2] Elixir Aircraft n.d. https://elixir-aircraft.com/en/.

[3] Carlsson LA, Kardomateas GA. Structural and Failure Mechanics of Sandwich Composites. Solid Mechanics and its Applications; 2011. https://doi.org/10.1007/978-1-4020-3225-7.

[4] Ley RP, Lin W, Mbanefo U. Facesheet wrinkling in sandwich structures. vol. CR-1999-20. 1999.

[5] Hoff NJ, Mautner SE. The Buckling of Sandwich-Type Panels. J Aeronaut Sci 1945;12:285–97. https://doi.org/10.2514/8.11246.

[6] Allen HG. Wrinkling and other forms of local instability. In: Neal B., editor. Anal. Des. Struct. Sandw. Panels. Pergamon P, 1969. https://doi.org/10.1016/b978-0-08-012870-2.50012-2.

[7] Sullins RT, Smith GW, Spier EE. Manual for structural stability analysis of sandwich plates and shells. NASA Contract Reports 1969.

[8] Zenkert D. The handbook of the sandwich construction. Engineering Materials Advisory Services.; 1997.

[9] Niu K, Talreja R. Modeling of wrinkling in sandwich panels under compression. J Eng Mech 1999;125:875–83. https://doi.org/10.1061/(ASCE)0733-9399(1999)125:8(875).

[10] Léotoing L, Drapier S, Vautrin A. Nonlinear interaction of geometrical and material properties in sandwich beam instabilities. Int J Solids Struct 2002;39:3717–39. https://doi.org/10.1016/S0020-7683(02)00181-6.

[11] Douville MA, Le Grognec P. Exact analytical solutions for the local and global buckling of sandwich beam-columns under various loadings. Int J Solids Struct 2013;50:2597–609. https://doi.org/10.1016/j.ijsolstr.2013.04.013.

[12] Ginot M, D'Ottavio M, Polit O, Bouvet C, Castanié B. Benchmark of wrinkling formulae and methods for pre-sizing of aircraft lightweight sandwich structures. Compos Struct 2021;273:114387. https://doi.org/10.1016/j.compstruct.2021.114387.

[13] D'Ottavio M. A Sublaminate Generalized Unified Formulation for the analysis of composite structures. Compos Struct 2016;142:187–99. https://doi.org/10.1016/j.compstruct.2016.01.087.

[14] Yu K, Hu H, Tang H, Giunta G, Potier-Ferry M, Belouettar S. A novel two-dimensional finite element to study the instability phenomena of sandwich plates. Comput Methods Appl Mech Eng 2015;283:1117–37. https://doi.org/10.1016/j.cma.2014.08.006.

[15] Choe J, Huang Q, Yang J, Hu H. An efficient approach to investigate the post-buckling behaviors of sandwich structures. Compos Struct 2018;201:377–88. https://doi.org/10.1016/j.compstruct.2018.06.025.

[16] D'Ottavio M, Polit O, Ji W, Waas AM. Benchmark solutions and assessment of variable kinematics models for global and local buckling of sandwich struts. Compos Struct 2016. https://doi.org/10.1016/j.compstruct.2016.01.019.

[17] Koissin V, Shipsha A, Skvortsov V. Effect of physical nonlinearity on local buckling in

sandwich beams. J Sandw Struct Mater 2010;12:477–94. https://doi.org/10.1177/1099636209104521.

[18] Fagerberg L. Wrinkling and compression failure transition in sandwich panels. J Sandw Struct Mater 2004;6:129–44. https://doi.org/10.1177/1099636204030475.

[19] Kassapoglou C, Fantle SC, Chou JC. Wrinkling of composite sandwich structures under compression. J Compos Technol Res 1995;17:308–16. https://doi.org/10.1520/ctr10451j.

[20] Fagerberg L, Zenkert D. Effects of anisotropy and multiaxial loading on the wrinkling of sandwich panels. J Sandw Struct Mater 2005;7:177–94. https://doi.org/10.1177/109963205048525.

[21] Oluwabusi OE, Toubia EA. In-Plane Shear Characterization of Composite GFRP-Foam Sandwich Panels. J Compos Constr 2019;23:04019034. https://doi.org/10.1061/(asce)cc.1943-5614.0000959.

[22] Rouchon J. Certification of large airplane composite structures, recent progress and new trends in compliance philosophy. 17th ICAS Congr 1990;1:1439–47.

[23] Laustsen S, Lund E, Kühlmeier L, Thomsen OT. Failure behaviour of grid-scored foam cored composite sandwich panels for wind turbine blades subjected to realistic multiaxial loading conditions. J Sandw Struct Mater 2014;16:481–510. https://doi.org/10.1177/1099636214541367.

[24] Serra J, Pierré JE, Passieux JC, Périé JN, Bouvet C, Castanié B. Validation and modeling of aeronautical composite structures subjected to combined loadings: The VERTEX project. Part 1: Experimental setup, FE-DIC instrumentation and procedures. Compos

Struct 2017;179:224–44. https://doi.org/10.1016/j.compstruct.2017.07.080.

[25] Serra J, Pierré JE, Passieux JC, Périé JN, Bouvet C, Castanié B, et al. Validation and modeling of aeronautical composite structures subjected to combined loadings: The VERTEX project. Part 2: Load envelopes for the assessment of panels with large notches. Compos Struct 2017;180:550–67. https://doi.org/10.1016/j.compstruct.2017.08.055.

[26] ANR VERTEX Program. 30 March 2020 n.d. https://www.institut-clement-ader.org/vertex/.

[27] Yang QD, Cox BN, Fang XJ, Zhou ZQ. Virtual testing for advanced aerospace composites: Advances and future needs. J Eng Mater Technol Trans ASME 2011;133:1–6. https://doi.org/10.1115/1.4002637.

[28] Peters RW. BUCKLING TESTS OF FLAT RECTANGULAR PLATES UNDER COMBINED SHEAR AND LONGITUDINAL COMPRESSION. NACA, Tech Note 1948;194:130. https://doi.org/10.1016/s0016-0032(22)90049-3.

[29] Klein H. Genera about Buckling tests with thin-walled shells. DLR-Mitt89-13 n.d.

[30] Castanié B, Barrau JJ, Jaouen JP. Theoretical and experimental analysis of asymmetric sandwich structures. Compos Struct 2002;55:295–306. https://doi.org/10.1016/S0263-8223(01)00156-8.

[31] Castanié B, Barrau JJ, Jaouen JP, Rivallant S. Combined shear/compression structural testing of asymmetric sandwich structures. Exp Mech 2004;44:461–72. https://doi.org/10.1177/0014485104047607.

[32] Bergan A, Bakuckas JG, Lovejoy A, Jegley D, Linton K, Korkosz G, et al. Full-scale test and analysis results of a PRSEUS fuselage panel to assess damage containment features.

Aircr. Airworth. Sustain. Conf., 2011, p. 1–17.

[33] Serra J. Étude expérimentale et numérique de la propagation de coupure dans des stratifés composites soumis à des chargements complexes. Université de Toulouse, 2016.

[34] Trellu A, Pichon G, Bouvet C, Rivallant S, Castanié B, Serra J, et al. Combined loadings after medium velocity impact on large CFRP laminate plates: Tests and enhanced computation/testing dialogue. Compos Sci Technol 2020;196:23. https://doi.org/10.1016/j.compscitech.2020.108194.

[35] Allen HG, Zhengnong F. Classification of structural sandwich panel behaviour. In: Vautrin A, editor. Proc. EUROMECH 360 Colloq., Saint Etienne: 1997, p. 1–12.

[36] Bozhevolnaya E, Thomsen OT, Kildegaard A, Skvortsov V. Local effects across core junctions in sandwich panels. Compos Part B Eng 2003;34:509–17. https://doi.org/10.1016/S1359-8368(03)00043-X.

[37] Fagerberg L, Zenkert D. Imperfection-induced wrinkling material failure in sandwich panels. J Sandw Struct Mater 2005;7:195–219. https://doi.org/10.1177/1099636205048526.

[38] Castanié B, Aminanda Y, Bouvet C, Barrau JJ. Core crush criterion to determine the strength of sandwich composite structures subjected to compression after impact. Compos Struct 2008;86:243–50. https://doi.org/10.1016/j.compstruct.2008.03.032.

[39] Birman V, Bert CW. Wrinkling of composite-facing sandwich panels under biaxial loading. J Sandw Struct Mater 2004;6:217–37. https://doi.org/10.1177/1099636204033643.

[40] Vescovini R, D'Ottavio M, Dozio L, Polit O. Buckling and wrinkling of anisotropic sandwich plates. Int J Eng Sci 2018;130:136–56. https://doi.org/10.1016/j.ijengsci.2018.05.010.

[41] VIC-3D Correlated Solutions. VIC-3D Software Manual. n.d.

CRediT author statement

Malo Ginot: Investigation, Methodology, Validation, Writing - Original Draft, Review & Editing

Bruno Castanié: Conceptualization, Supervision, Review & Editing,

Christophe Bouvet: Conceptualization, Supervision, Review & Editing,

Joel Serra: Testing, Supervision,

Nicolas Mahuet : Industrial Supervision

Declaration of interests

☒ The authors declare that they have no known competing financial interests or personal relationships that could have appeared to influence the work reported in this paper.

☐The authors declare the following financial interests/personal relationships which may be considered as potential competing interests:

M. Ginot, C. Bouvet, B. Castanié, J. Serra, N. Mahuet